SANDIA REPORT
SAND2022-13014
Printed September 2022

FY22 Progress on Imbibition Testing in Containment Science

Kristopher L. Kuhlman, Forest T. Good, Tara LaForce, Jason E. Heath

Prepared by
Sandia National Laboratories
Albuquerque, New Mexico
87185 and Livermore,
California 94550

Issued by Sandia National Laboratories, operated for the United States Department of Energy by National Technology & Engineering Solutions of Sandia, LLC.

Available to DOE and DOE contractors from
U.S. Department of Energy
Office of Scientific and Technical Information
P.O. Box 62
Oak Ridge, TN 37831

Telephone: (865) 576-8401
Facsimile: (865) 576-5728
E-Mail: reports@osti.gov
Online ordering: http://www.osti.gov/scitech

Available to the public from
U.S. Department of Commerce
National Technical Information Service
5301 Shawnee Rd
Alexandria, VA 22312

Telephone: (800) 553-6847
Facsimile: (703) 605-6900
E-Mail: orders@ntis.gov
Online order: https://classic.ntis.gov/help/order-methods/

ABSTRACT

Estimation of two-phase fluid flow properties is important to understand and predict water and gas movement through the vadose zone for agricultural, hydrogeological, and engineering applications, such as for vapor-phase contaminant transport and/or containment of noble gases in the subsurface. In this second progress report of FY22, we present two ongoing activities related to imbibition testing on volcanic rock samples. We present the development of a new analytical solution predicting the temperature response observed during imbibition into dry samples, as discussed in our previous first progress report for FY22. We also illustrate the use of a multi-modal capillary pressure distribution to simulate both early- and late-time imbibition data collected on tuff core that can exhibit multiple pore types. These FY22 imbibition tests were conducted for an extended period (i.e., far beyond the time required for the wetting front to reach the top of the sample), which is necessary for parameter estimation and characterization of two different pore types within the samples.

ACKNOWLEDGEMENTS

This research was funded by the National Nuclear Security Administration, Defense Nuclear Nonproliferation Research and Development (NNSA DNN R&D). The authors acknowledge important interdisciplinary collaboration with scientists and engineers from Los Alamos National Laboratory, Lawrence Livermore National Laboratory, Mission Support & Test Services, Pacific Northwest National Laboratory, and Sandia National Laboratories (SNL). The authors thank Scott Broome (SNL) for support of this ongoing work under the Containment Venture at Sandia, and they thank Michael Nole (SNL) for technically reviewing the report.

CONTENTS

LIST OF FIGURES

ACRONYMS AND TERMS

Acronym/Term	Definition
FY	fiscal year
NNSS	Nevada National Security Site
PFLOTRAN	parallel flow and transport (https://pflotran.org/)
RTD	resistance temperature detector
YMP	Yucca Mountain Project

1. INTRODUCTION

Estimation of two-phase fluid flow properties is important to understand and predict both water and gas flow through the vadose zone for agricultural, hydrogeological, and engineering applications such as vapor-phase contaminant transport and/or containment of noble gases in the subsurface. To estimate properties and subsequently predict physically realistic processes, laboratory experiments of spontaneous water imbibition with simultaneous temperature measurement and modeling via numerical and analytical methods of the results are developed and discussed in this report.

This report updates progress on, improvement to, and application of laboratory methods first developed in fiscal year 2021 (FY21; Kuhlman & Heath, 2021) and reported on earlier this FY (Kuhlman et al., 2022b) for measurement of spontaneous water imbibition into large core samples (e.g., ~ 6 cm diameter by ~ 10 cm long). In this report we present two ongoing activities related to imbibition testing:

- development of an analytical solution to predict the temperature response observed during imbibition into dry samples, as first discussed earlier this FY (Kuhlman et al., 2022b); and
- illustration of the use of a multi-modal capillary pressure distribution to simulate both early- and late-time data collected in recent imbibition tests conducted on core collected as part of the site characterization effort in P-Tunnel at the Nevada National Security Site (NNSS).

Compared to imbibition tests in FY21 on NNSS core from other stratigraphic horizons (Kuhlman et al., 2021), these FY22 imbibition tests were conducted for an extended period (i.e., far beyond the time required for the wetting front to reach the top of the sample), providing imbibition data to characterize two different pore types within the samples.

The details of the laboratory experimental setup are discussed in an earlier report (Kuhlman et al., 2022b). The following discussion uses an alternative approach to simulate the multiporosity nature of the rock during water imbibition. Finally, we discuss future steps being carried out this year and next year as part of the ongoing investigation into the hydrogeology of containment science.

2. LABORATORY EXPERIMENT

From 8 to 12 July 2022, an extended laboratory spontaneous imbibition experiment was performed on a zeolitic tuff core sample from P-Tunnel at Aqueduct Mesa, Nevada. The zeolitic tuff sample is identified as "U12p06 GI-4D 46.0-46.4" (equivalently "4D-46Z" in the abbreviated convention; "4D" is the borehole, the number is the depth in the borehole in feet and "Z" indicates zeolitic). This is a repeat of the test conducted in March 2022 and reported in Kuhlman et al. (2022b), but the sample was jacketed to reduce temperature loss and potentially outward/inward vapor transport along the sides of the core, based on lessons learned from thermal modeling with the analytical solutions presented later in this report (see Section 4).

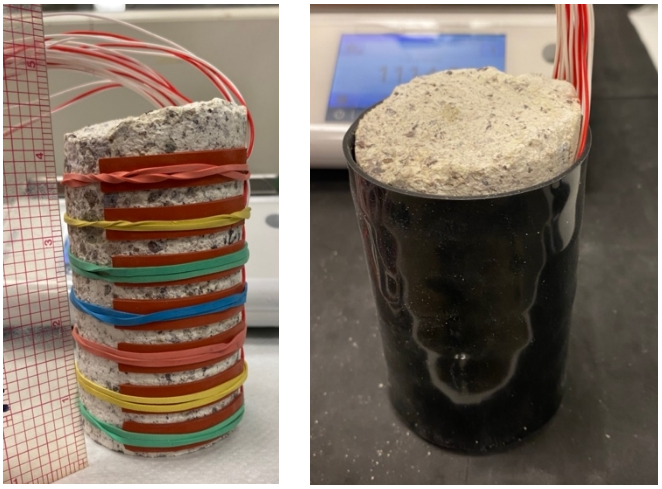

Figure 1. Sample 4D-46Z before jacketing showing seven resistance temperature detectors (RTDs) (left) and after jacketing (right).

The balance was monitored at 0.1 Hz (Figure 2) and temperatures were recorded at seven heights using resistance temperature detectors (RTDs) along the length core at 2 Hz (Figure 3). Adsorption of water onto the rock surface of a dry porous medium is exothermic (i.e., releases a small heat pulse), analogous to the latent heat released when liquid water condenses from steam. This occurs because free water is converted to bound water in a dry porous medium, a process referred to as the "heat of wetting" (Edlefesen & Anderson, 1943), "sorptive heating" (Murali et al., 2020), or the "latent heat of adsorption" (Aslannejad et al., 2017).

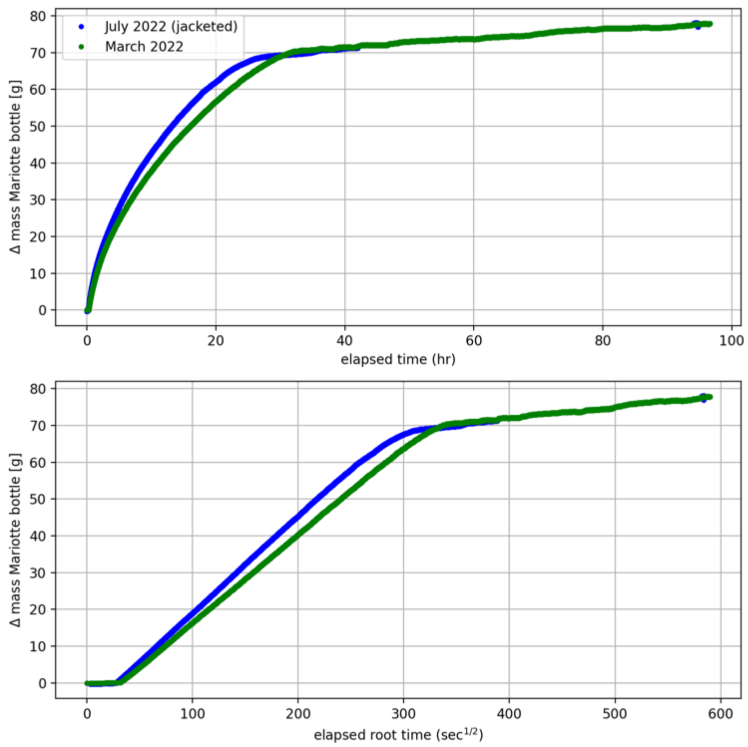

Figure 2. Mass imbibed data collected using a Python script during two spontaneous imbibition tests on sample 4D-46Z. Top: linear time axis; Bottom: same data on square root time axis.

The mass imbibed time series, recorded from the balance, is shown in Figure 2 for both a linear time scale and the diagnostic square root of time scale. Spontaneous imbibition is well-known to plot linearly against the square root of time (Philip 1957; Tokunaga, 2020). The early-time flat portion of the data, more visible in the root-time plot, is associated with the sample imbibing the standing water in the sample holder before it draws more water in from the Mariotte bottle.

The origin of the difference between the March and July test may partially be due to ambient lab temperature and ambient lab relative humidity (RH). A slight increase in temperature in July as compared to March (~2 °C) would be associated with a reduction in the viscosity of water (~5%) which explains some of the observed difference between the tests. The July test has a steeper mass imbibed slope than the March test, which would be associated with a higher mobility (fluid relative permeability divided by fluid viscosity). The ambient RH in July is higher (due to monsoon season in Albuquerque) than in March. The test likely started drier in March, than in July.

The thermal response of the RTDs at early time for the July 2022 test is shown in Figure 3, and the responses during the entire spontaneous imbibition test are shown in Figure 4. The effect of the building's heating and cooling system in the lab (823/B59) is evident in the late-time data for both tests, which each show approximately 0.5 °C daily fluctuations, despite covering the sample holder with a bag and covering the entire experiment with a polycarbonate box. Both the March 2022 experiment and the July 2022 experiment are shown in Figure 4.

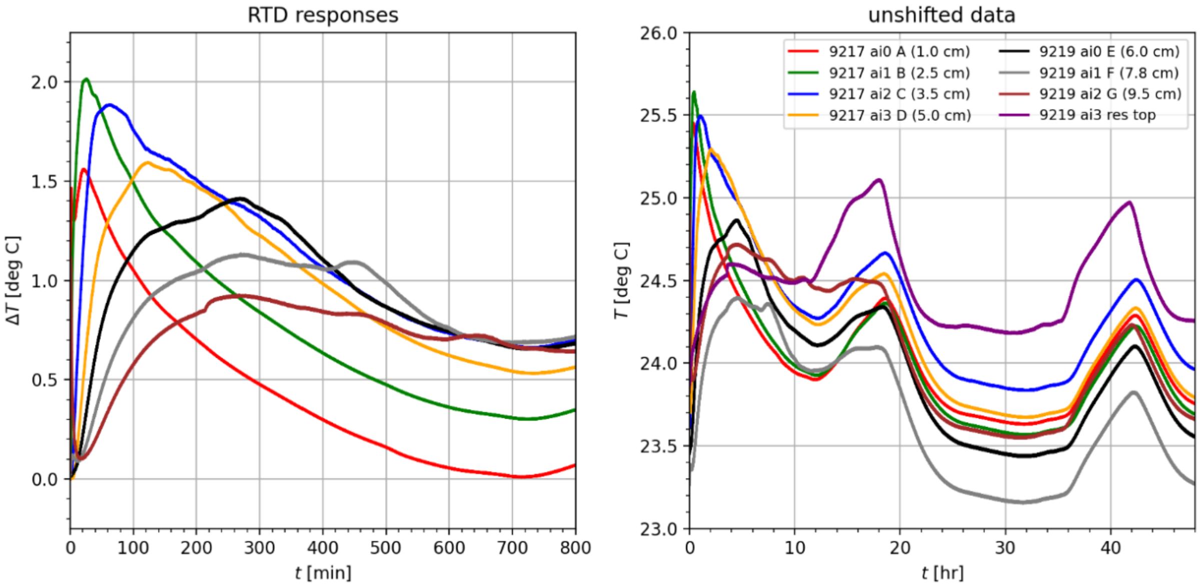

Figure 3. Temperature data collected using National Instruments LabVIEW during the July 2022 4D-46Z spontaneous imbibition test. Left: relative temperature (change from initial) at early time (<800 min) for 7 monitoring locations on core; Right: unshifted data.

The analytical solution presented later in this report (see Section 4) will eventually be used to fit observations of temperature change and constrain the rock thermal properties.

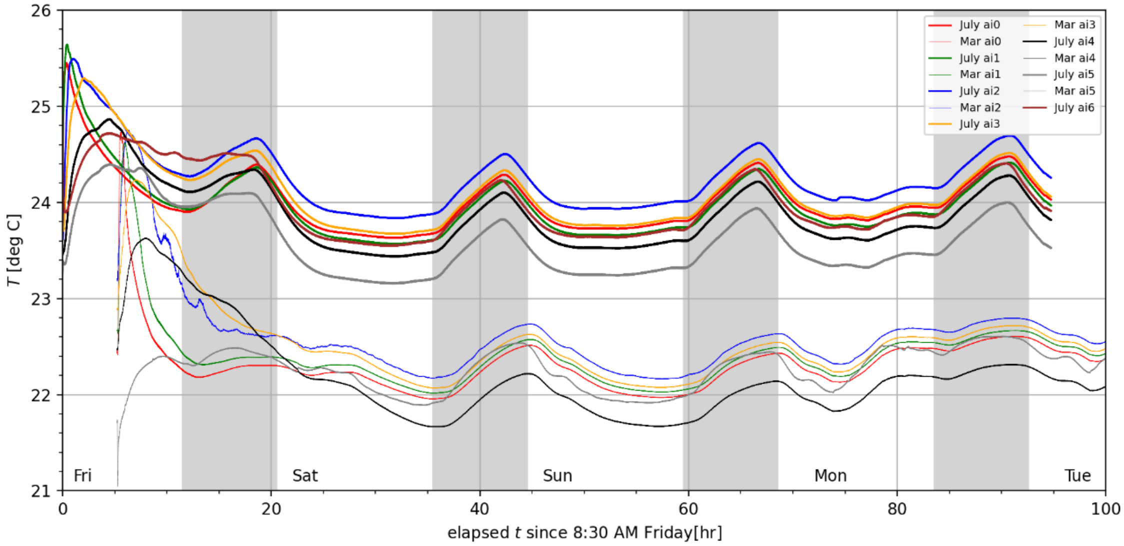

Figure 4. Temperature data during both multi-day 4D-46Z spontaneous imbibition tests. Gray bars indicate 8 PM to 5 AM each day. March 2022 test (thinner lines) started at 12:50 PM; July 2022 test (thicker lines) started at 8:30 AM.

Many of the differences between the two tests were due to the time of year. The temperature was on average two degrees warmer in July than in March, and the RH of the air was higher in July (~40%) than in March (<20%). Photography of the wetting front was not possible for this re-test, due to the black rubber jacket.

3. MULTIMODAL PORE DISTRIBUTIONS

Using a single-porosity flow model, the late-time mass-imbibed data are predicted to be constant (i.e., no additional inflow of water after the wetting front reaches the top of the sample). In a previous report (Kuhlman et al., 2022b), we showed how the late-time slope (i.e., after the water table has reached the top of the sample) observed in imbibition test results could be matched with a multicontinuum model. This multiporosity conceptual model treats the rock as consisting of two overlapping continua, each with its own physical properties, including permeability, porosity, and capillary pressure and relative permeability curves.

Here we present an alternative approach to matching the two observed slopes in the mass imbibed data (i.e., bottom subplot of Figure 2), which is like the approach used to model previous imbibition tests conducted as part of the Yucca Mountain Project (Peters et al., 1987; Peters & Klavetter, 1988). The late-time slope of the mass-imbibed data in these historic tests (Figure 5, left) are like the late-time data observed in recent tests. Peters et al. (1987) constructed an ad hoc capillary pressure curve (i.e., "constructed function" in Figure 5, right) for use in numerical models to best-fit observations. Here, we propose a flexible functional form to allow automatic parameter estimation of multimodal distribution parameters.

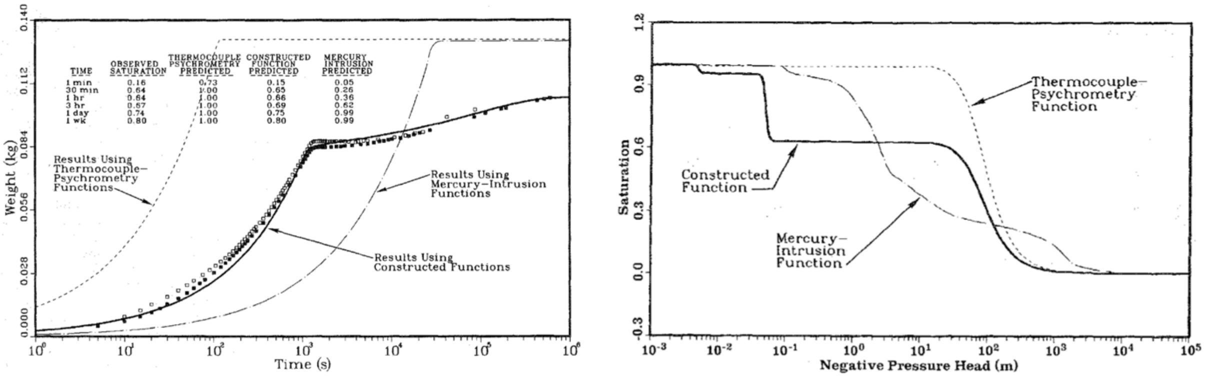

TIME	OBSERVED SATURATION	THERMOCOUPLE PSYCHROMETRY PREDICTED	CONSTRUCTED FUNCTION PREDICTED	MERCURY INTRUSION PREDICTED
1 min	0.16	0.73	0.15	0.05
30 min	0.64	1.00	0.65	0.26
1 hr	0.64	1.00	0.66	0.36
3 hr	0.67	1.00	0.69	0.62
1 day	0.74	1.00	0.75	0.99
1 wk	0.80	1.00	0.80	0.99

Figure 5. Mass imbibed response (left) and constructed capillary pressure curve (right) for imbibition into volcanic tuff (Peters et al., 1987).

The multimodal approach uses an extension to the multimodal form of the widely used unimodal van Genuchten (1980) curve proposed by Priesack and Durner (2006). Their original form was used by Heath et al. (2021) to fit to mercury intrusion capillary pressure (MICP) test data on 19 core samples from the NNSS. We use a modified form that is more like the form implemented in PFLOTRAN for the unimodal van Genuchten (1980) model and its extension to two-phase flow by Parker et al. (1987). The multimodal model we implemented for two-phase flow of water and gas is of the following form

$$S_e = \sum_{i=1}^{N} w_i \left[1 + (p_c \alpha_i)^{\frac{1}{1-m_i}} \right]^{-m_i} \tag{1}$$

$$k_{rl} = \sqrt{S_e} \left\{ \frac{\sum_{i=1}^{N} w_i \alpha_i \left[1 - \left(1 - S_e^{\frac{1}{m_i}} \right)^{m_i} \right]}{\sum_{i=1}^{N} w_i \alpha_i} \right\}^2 \tag{2}$$

$$k_{rg} = \sqrt{1 - S_e} \left[\frac{\sum_{i=1}^{N} w_i \alpha_i \left(1 - S_e^{\frac{1}{m_i}} \right)^{2m_i}}{\sum_{i=1}^{N} w_i \alpha_i} \right] \tag{3}$$

where S_e is the dimensionless effective saturation, k_{rl} and k_{rg} are the dimensionless relative permeabilities for liquid and gas phases, N is the number of modes (i.e., porosities), w is a dimensionless weight factor, m is the dimensionless van Genuchten exponent, α is the van Genuchten capillary pressure scaling factor [$1/\mathrm{Pa}$] (also known as the inverse air-entry pressure), and p_c is the capillary pressure [Pa]. The form of the effective saturation (1) comes directly from Priesack and Durner (2006), but the liquid relative permeability model (2) is modified, and the gas relative permeability model (3) draws on analogy with the modified liquid relative permeability model. An implementation of this distribution is illustrated in Figure 6.

This general functional form is not currently implemented directly in PFLOTRAN (Hammond et al., 2014), and thus it is implemented here through a table of values with linear interpolation. These functions are implemented externally (i.e., a Python or MATLAB script), and a text file table is created and imported via the PFLOTRAN input file. PFLOTRAN further requires the tables to be written in the functional form $p_c(S_e)$, rather than $S_e(p_c)$ as shown in Equation 1 above. The unimodal van Genuchten (1980) model can readily be inverted algebraically, but the more general multimodal model is here inverted numerically through interpolation.

The early-time mass imbibed data are associated with the drier end of the capillary pressure curve (dictated by m_1 and α_1 in Figure 6), while the late-time mass imbibed data (after 350 sqrt(sec) in Figure 7) are associated with the wetter end of the capillary pressure curve (dictated by m_2 and α_2). The balance or break between the two curves is adjusted by the two weights ($\sum_i w_i = 1$).

This multi-modal approach for multiporosity porous media is more efficient than the more general multicontinuum approach given in Kuhlman et al. (2022b), but currently it only works to represent a multiporosity fluid flow response in water imbibed data—that is, a multiporosity thermal response and a multiporosity transport response would also be required for energy and solute transport. Basically, the constitutive laws need to be constructed to accommodate the multiporosity nature of the rocks for the given set of physics being modeled, and thus geomechanics could theoretically also be represented with multimodal approaches. In contrast, the multicontinuum approach with multiple overlapping continua that do not have multimodal constitutive laws can represent multiporosity systems with fluid flow, heat flow, solute transport, and potentially mechanical deformation as long as the governing equations include those processes, and thus each continuum represents a single unimodal porosity type of the multiporosity system. The multi-modal multiporosity approach will allow more efficient estimation of two-phase fluid flow properties using automated parameter estimation, which requires efficient forward model execution.

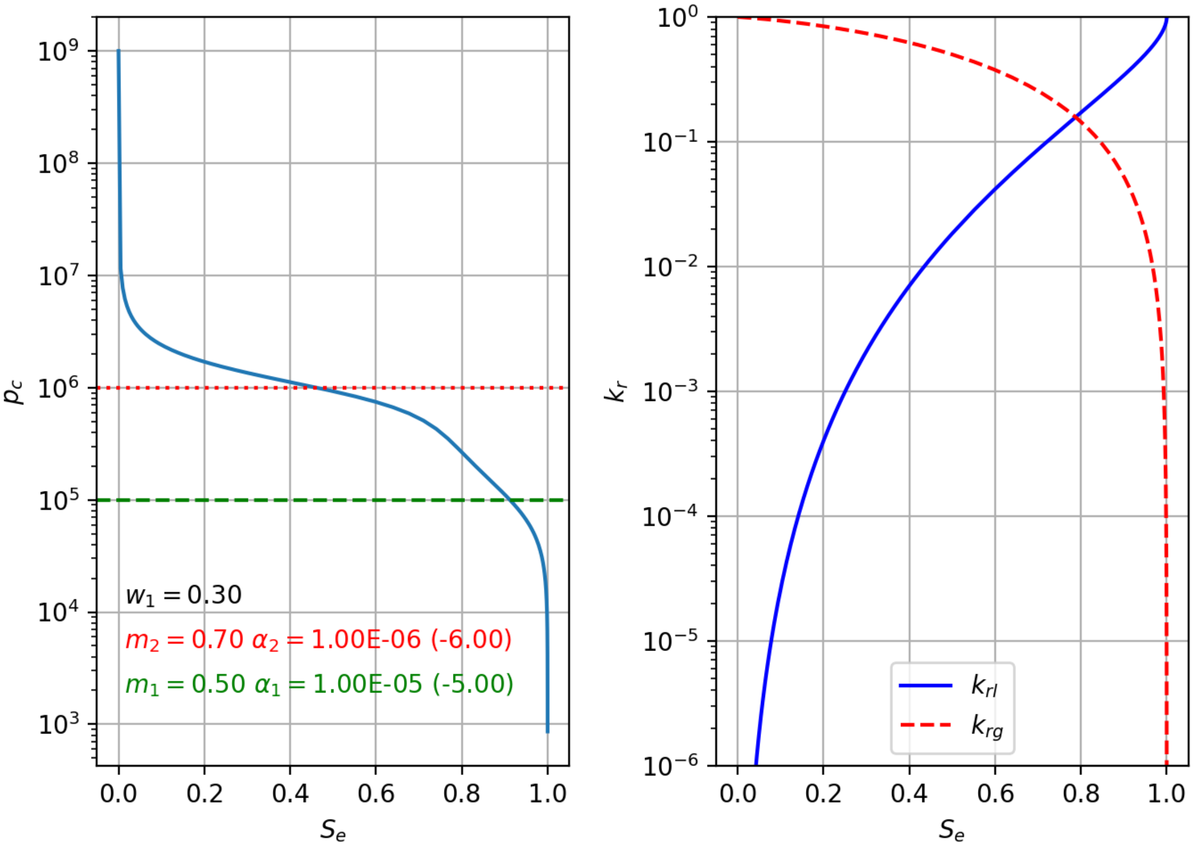

Figure 6. Bi-modal modified Priesack & Durner (2006) model, given by Equations (1-3). Left: moisture retention curve with air-entry pressures indicated (horizontal lines) for the two porosity types of the bi-modal system; Right: relative permeability curves for liquid and gas.

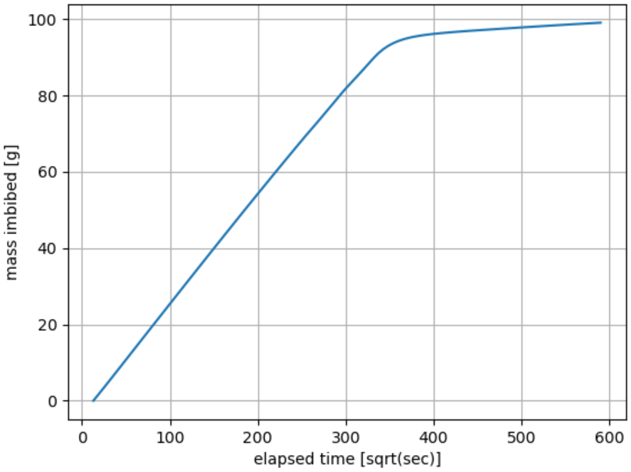

Figure 7. PFLOTRAN prediction of imbibition response with late-time mass imbibed slope (after 350 sqrt(sec)), using the bi-modal model given in Figure 6.

4. THERMAL MODEL DEVELOPMENT

This section provides a narrative on the development of an analytical solution to describe the observed thermal response described in the previous sections. We discuss the different methods investigated and their gradual improvement to illustrate the development process.

4.1. Moving Point Source Model

The observed rise in temperature during spontaneous imbibition is hypothesized to be the result of the heat produced as the rock is wetted, known as the 'heat of wetting' (Edlefesen & Anderson, 1943) or the 'latent heat of sorption' (Aslannejad et al., 2017). The sorbing water on the leading edge of the wetting front is the source of this heat. While the wetting front has some width, it is simplest to first consider it as a source of heat of infinitesimally small width. That is, a good approximation for the heat produced by the wetting front is the Dirac delta function, which is defined as

$$\delta(x-a) = 0; x \neq a$$
$$\int_{-\infty}^{\infty} \delta(x-a)\,\mathrm{d}x = 1.$$

The Dirac delta function carries an impulse of unit magnitude at $x = a$ and has dimensions equal to the inverse of its argument. Two useful properties of the Dirac delta function are

$$\int_a^c f(x)\delta(x-b)\,\mathrm{d}x = \begin{cases} 0; & \text{if } b \notin [a,c] \\ f(b); & \text{if } b \in [a,c] \end{cases} \tag{4a}$$

$$\delta(k(x-b)) = \frac{1}{|k|}\delta(x-b) \tag{4b}$$

Consider the one-dimensional transient heat conduction equation along an infinite domain with a constant point heat source moving at a constant speed *u* in the positive x direction. The temperature T [K] can be modeled with the transient heat conduction equation with a source term and a loss term to the surroundings:

$$\frac{\partial^2 T}{\partial x^2} + \frac{1}{k} g_D(x,t) = \frac{1}{\alpha_T}\frac{\partial T}{\partial t} + \frac{Ph}{kA}T$$

where k is the porous medium bulk thermal conductivity $[\mathrm{W/(m \cdot K)}]$, α_T is the porous medium thermal diffusivity $[\mathrm{m^2/s}]$, P and A are the perimeter [m] and cross-sectional area $[\mathrm{m^2}]$ of the rock, h is the heat transfer coefficient for heat loss to the lateral surfaces of the rock due to the surroundings $[\mathrm{W/(m^2 \cdot K)}]$, and g_D is the heat source term $[\mathrm{W/m^2}]$ given by

$$g_D(x,t) = G\delta(x-ut)$$

where G is a constant that represents the strength of the heat source.

This problem is taken from the welding literature and was solved by Özişik (1993) through a similarity transform into a new coordinate axis $\xi = x - ut$ [m] that moves with the heat source at speed u [m/s]. The solution has no boundaries (i.e., continues to infinity in both directions) or initial conditions and utilizes a dynamic steady-state assumption; since the temperature does not change significantly in the moving coordinate system, the time derivative can be eliminated which simplifies the equation to an ordinary differential equation (ODE). The domain is split into two regions on either side of the heat source that are then solved independently. The unknown constants in the two solutions are solved for by ensuring the continuity of temperature at the boundary and by ensuring the ‘jump condition’ is met. This results in the solution

$$T_1(\xi) = Ce^{\left(m_1 - \frac{u}{2\alpha_{T1}}\right)\xi}; \quad \xi < 0$$

$$T_2(\xi) = Ce^{-\left(m_2 + \frac{u}{2\alpha_{T2}}\right)\xi}; \quad \xi > 0$$

$$C = G\left[k_1\left(m_1 - \frac{u}{2\alpha_{T1}}\right) + k_2\left(m_2 + \frac{u}{2\alpha_{T2}}\right)\right]^{-1}$$

$$m_i = \sqrt{\left(\frac{u}{2\alpha_{Ti}}\right)^2 + \frac{Ph}{k_i A}}. \tag{5}$$

where subscript 1 refers to the region to the left and subscript 2 to the region to the right of the wetting front. This solution allows different thermal properties (k and $\underline{\alpha}_T$) on either side of the wetting front (thermal properties are often considered to be a function of water saturation, e.g., see Somerton et al., 1974). A plot of the solution in both the space and time domains with arbitrary constants is shown in Figure 8.

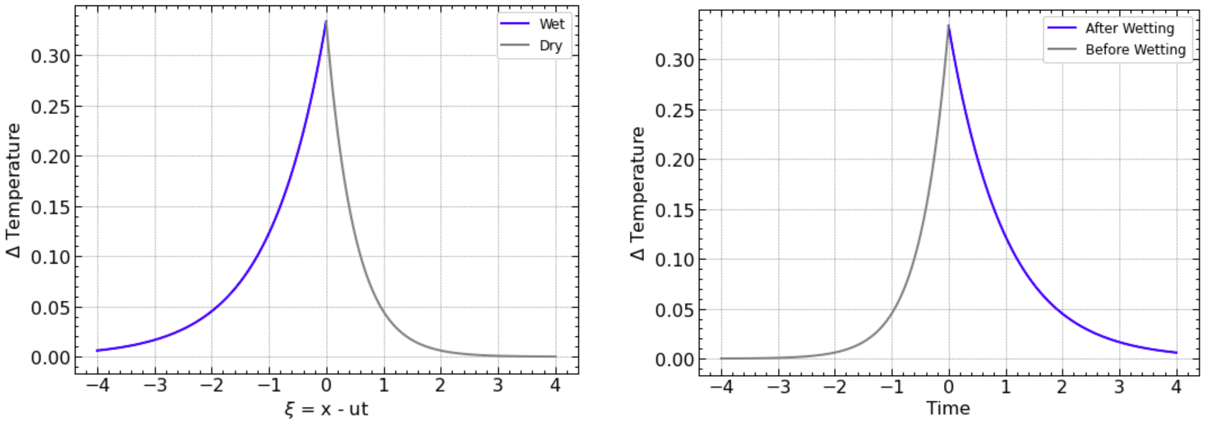

Figure 8. Change in temperature for the moving delta function solution, showing space (left) and time (right) profiles.

The predicted curves qualitatively produce a general shape of the temperature data observed during spontaneous imbibition (Figure 3). In the time domain, the curve is characterized by a sharp rise in temperature to a maximum followed by a slower decline. The asymmetry in the peak in the analytical solution is due to two reasons: 1) the assumption of uniform velocity of the wetting front; and 2) a higher thermal conductivity of the saturated rock behind the wetting front makes the material conduct less into the dry part of the formation. The real phenomenon also contains an additional cause of asymmetry: due to the square root time dependence of the position of the wetting front, the wetting front does not move at constant speed, but is slowing down. This behavior would stretch the right sub-plot of Figure 8.

There are several discrepancies between this model and the phenomenon in reality:

1. The model contains a sharp peak, whereas the data contain more rounded peaks. This is because the physical heat source has a finite width and is not infinitesimally narrow.
2. The speed of the wetting front should change over time and not be constant. This would eliminate the possibility of utilizing the quasi-stationary condition, since the temperature in the moving coordinate axis would change with time.
3. Core-scale heterogeneity: exchange of fluid between different multiporosity types (minerals could have different release of energy during sorption of water; the release of energy tends to be proportional to the specific surface area)—a multimodal or mutlicontinuum extension may be needed.

The following improvement attempts to fix some of these shortcomings.

4.1.1. Moving 'Boxcar' Source Model

To spread out the heat source from the previous solution, we consider a heat source defined by:

$$g_{BC}(x,t) = GB_w(\xi)$$

where B_w is an impulse function with unit area defined as

$$B_w = \begin{matrix} 0 & ;\xi < -w/2 \\ 1/w & ;-\frac{w}{2} < \xi < \frac{w}{2}. \\ 0 & ;\xi > w/2 \end{matrix}$$

where w is the width [m] of the pulse. The Dirac delta function is a special case of this function where the limit is taken as $w \rightarrow 0$. This Boxcar function better represents a wetting front with non-zero width.

The heat conduction equation with the updated Boxcar heat source term can be solved in a similar manner to the previous problem. However, the domain must be divided into 3 regions, namely, the 3 regions specified in the definition of B_w. The solutions for the three regions are:

$$T_1(\xi) = C_1 e^{\left[m_1 - \frac{u}{2\alpha_{T1}}\right]\xi} \qquad \xi < \; -w/2$$

$$T_2(\xi) = C_2 e^{-\left[m_2 + \frac{u}{2\alpha_{T2}}\right]\xi} + C_3 e^{\left[m_3 - \frac{u}{2\alpha_{T3}}\right]\xi} + \frac{GA}{wPh} \qquad -w/2 < \; \xi < w/2$$

$$T_3(\xi) = C_4 e^{-\left[m_3 + \frac{u}{2\alpha_{T3}}\right]\xi} \qquad \xi > w/2.$$

By setting $T_1\left(-\frac{w}{2}\right) = T_2\left(-\frac{w}{2}\right)$ and $T_2\left(\frac{w}{2}\right) = T_3\left(\frac{w}{2}\right)$, and using the previous definition for m_i, (Equation 5) the free constants (C_i) can be determined.

To obtain a proper energy balance at the boundaries of the three regions, the thermal conductivity must be continuous across the domain. If a difference in conductivity between regions 1 and 3 is desired, then region 2 must contain a space-dependent thermal conductivity that connects the conductivities of regions 1 and 3. This would, of course, modify the solution of region 2, rendering the solution given above invalid for different conductivities in regions 1 and 3. However, if the energy balance at each of the individual boundaries is disregarded (in a case where the difference in heat flux on each side of the boundary is negligible), then an energy balance between regions 1 and 3 across the entirety of region 2 can be obtained by setting:

$$k_2 = \frac{k_1\left(m_1 - \frac{u}{2\alpha_{T1}}\right) + k_3\left(m_3 + \frac{u}{2\alpha_{T3}}\right)}{m_1 - \frac{u}{2\alpha_{T1}} + m_3 + \frac{u}{2\alpha_{T3}}}.$$

The characteristic shape of the solution in the time-domain is shown in Figure 9.

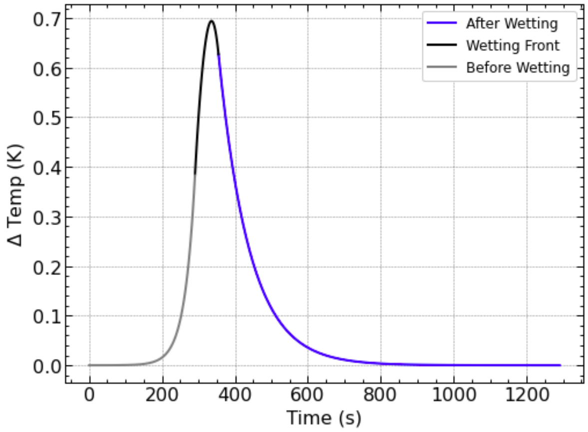

Figure 9. Temperature rise predicted for boxcar source in the time domain.

This model provides insight into a slightly more realistic model of the wetting front, which has some width. It produces curves more like the general shape of the curves from the zeolitic tuff data (Figure 3), which has rounded rather than sharp peaks. However, the parameter w controlling the width of the wetting front is not physically derived. It may be possible to obtain an estimate for the average width of the wetting front during the experiment, but this value varies over the course of the imbibition experiment (sharper or narrower wetting front at the start of the experiment and a more diffuse wetting front at the end). This parameter provides more of an aesthetic improvement in the approximation of the curve, rather than an improvement that captures a new aspect of the relevant physics. Given this information, a source term modeled with the Dirac delta function achieves most of the fundamental characteristics of the curve while being a more practical function to work with analytically.

4.2. Stefan Problem Approach

The process of spontaneous imbibition has some similarities to the Stefan problem from the phase-change literature (Carslaw & Jaeger, 1959; Özişik, 1993) describing the temperature of a medium undergoing a phase change. The phase change occurs at the moving interface between phases. The phase change includes latent heat released at the interface. The solution to the Stefan problem, therefore, describes both the temperature in the two regions as well as the position of the interface. Ignoring heat flow due to advection of water, the imbibition process contains both the moving interface and the release of latent heat at the interface. Therefore, a simplified model can be constructed using a solution to the Stefan problem.

The Neumann solution to the Stefan problem (Özişik, 1993) describes the temperature T and the position of the interface $s(t)$ in the semi-infinite domain $0 \leq x < \infty$ assuming not only continuity of temperature, but constant temperature (i.e., first type boundary condition) at the interface. The problem is formulated as

Solid phase	$\frac{\partial^2 T_s}{\partial x^2} = \frac{1}{\alpha_{Ts}} \frac{\partial T_s}{\partial t}, 0 < x < s(t), t > 0$ $T_s(0,t) = T_0$
Liquid phase	$\frac{\partial^2 T_l}{\partial x^2} = \frac{1}{\alpha_{Tl}} \frac{\partial T_l}{\partial t}, s(t) < x < \infty, t > 0$ $T_l(x,0) = T_i$ $\lim_{x \to \infty} T_l(x,t) = T_i$
Interface	$T_s(s(t),t) = T_l(s(t),t) = T_m$ $k_s \frac{\partial T_s}{\partial x} - k_l \frac{\partial T_l}{\partial x} = \rho H \frac{ds}{dt}$;at $x = s(t)$

where T_0 is the initial temperature of the solid phase, T_i is the initial temperature of the liquid phase, T_m is the fixed temperature at the interface, k_i is the thermal conductivity of region i (solid or liquid), α_i is the thermal diffusivity, ρ is the porous medium density [$\mathrm{kg/m^3}$], and H is the latent heat of the phase change [$\mathrm{J/kg}$] at the interface.

The second equation at the interface is known as the Stefan condition, which is essentially an energy balance stating that the outward heat flux at the interface must be equal to the rate of heat liberated at the interface. The rate of heat produced is proportional to the speed of the interface since the amount of heat produced is proportional to the amount of the medium which underwent a phase change.

The Neumann solution is given as

$$T_s(x,t) = (T_m - T_0)\frac{\mathrm{erf}\left(x/2(\alpha_s t)^{1/2}\right)}{\mathrm{erf}(\lambda)} + T_0$$

$$T_l(x,t) = (T_m - T_i)\frac{1 - \mathrm{erf}\left(x/2(\alpha_l t)^{1/2}\right)}{1 - \mathrm{erf}(\lambda(\alpha_s/\alpha_l)^{1/2})} + T_i$$

$$s(t) = 2\lambda(\alpha_s t)^{1/2}$$

where lambda is determined by solving the transcendental equation:

$$\frac{e^{-\lambda^2}}{\mathrm{erf}\,(\lambda)} + \frac{k_l}{k_s}\left(\frac{\alpha_{Ts}}{\alpha_{Tl}}\right)^{1/2} \frac{T_m - T_i}{T_m - T_0} \frac{e^{-\lambda(\alpha_{Ts}/\alpha_{Tl})}}{1 - \mathrm{erf}[\lambda(\alpha_{Ts}/\alpha_{Tl})^{1/2}]} = \frac{\lambda H \sqrt{\pi}}{c_p(T_m - T_0)}$$

Here c_p is the specific heat capacity [$\mathrm{J/(kg \cdot K)}$] and $\mathrm{erf}(z)$ is the error function [NIST, 2022, their equation 7.2.1]. We model the imbibition problem using this solution by treating the solid and liquid regions of the Stefan problem as the wetted and dry regions of the imbibition problem. Taking $T_0 = T_i = 0$, $T_m = 2$ K (a temperature increase above background), and using thermal properties of volcanic rocks, we produce the plots in Figure 10.

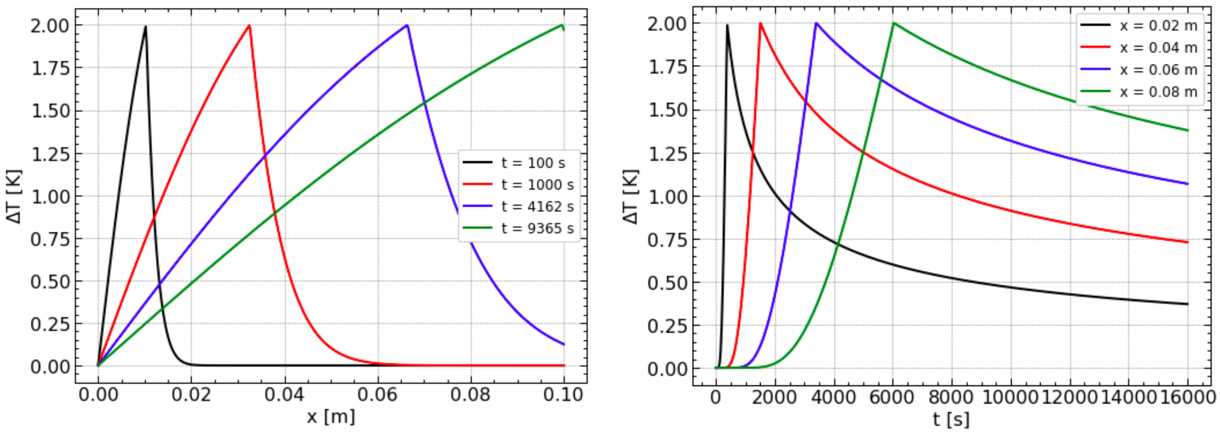

Figure 10. Temperature rise prediction for Stefan problem in space (left) and time (right) domains; $k_s = 0.79$ W/mK, $k_l = 0.253$ W/mK, $\rho = 1584$ kg/m³, $c_p = 1165$ J/kgK, and $H = 4000$ J/kg

The Stefan problem captures some aspects of the problem that were not captured in the previous models. First, it is formulated in the semi-infinite domain rather than the infinite domain which more accurately models the phenomenon since the imbibition process has a definite beginning at $x = 0$ and $t = 0$. Next, it defines the heat evolved at the boundary in terms of the latent heat of the 'phase change' as well as the speed of the wetting front. Finally, it allows for a non-constant speed of the wetting front, which is inherent in the imbibition problem. Using the same values as those used in the plots of Figure 10, the position of the wetting front height is given as $s(t) \approx \left(0.00103\ \frac{\mathrm{m}}{\sqrt{s}}\right)\sqrt{t}$. The height of the wetting front peak during spontaneous imbibition is known to be proportional to the square root of time (Philip, 1957; Tokunaga, 2020). The coefficient agrees to an order of magnitude to the imbibition rate deduced from the temperature peaks observed during imbibition into zeolitic tuff (0.0008 $\mathrm{m}/\sqrt{s}$).

However, there are some significant shortcomings of this model. The semi-infinite domain, while more accurate than the infinite domain, does not properly account for boundary effects at the far end of the core. Next, the Stefan problem has constant temperature at the interface, since the temperature associated with the phase change is known to be constant, at constant pressure. This is clearly not exhibited in the temperature rises observed in the zeolitic tuff data. A more complete model would account for variable yet continuous temperature at the interface, determined largely by the amount of heat released at the interface. The Stefan problem has a fixed temperature at an unknown location, while the imbibition problem has an unknown temperature at a known location (the wetting front).

4.3. Hybrid Stefan and Point Source Representation

Consider the one-dimensional heat conduction problem in the region $0 \leq x \leq L$ with a continuous moving point heat source associated with latent heat given by $g_{LH}(x,t)$:

$$\frac{\partial^2 T}{\partial x^2} + \frac{1}{k} g_{LH}(x,t) = \frac{1}{\alpha_T} \frac{\partial T}{\partial t} + \frac{Ph}{kA} T$$

$$-k\frac{\partial T}{\partial x}\bigg|_{x=0} + h_1T = 0$$

$$k\frac{\partial T}{\partial x}\bigg|_{x=L} + h_2T = 0$$

$$T(x,0) = 0$$

The problem is formulated with homogeneous third type boundary conditions, otherwise known as Robin boundary conditions, which prescribes the heat flux to be proportional to the temperature at the boundary with heat loss coefficient h_i. As h_i goes to infinity, the boundary condition reduces to the first type (Dirichlet) with fixed temperatures. As h_i goes to zero, the boundary condition is reduced to a homogeneous second type (Neumann) with fixed heat flux. In this formulation the thermal properties on either side of the wetting front are assumed to be the same (as opposed to the point source solution illustrated in the first subsection). In practice, the saturated rock would have slightly different values for thermal conductivity and diffusivity, but we assume that these differences are negligible.

This formulation of the problem is like the Stefan problem since the magnitude of the heat source is proportional to the speed of the moving interface. Instead of modelling the interface as a boundary where there is a supply of heat, the interface is modeled with a Dirac delta function proportional to the latent heat.

A heat source associated with the release of energy by latent heat is given by

$$g_{LH}(x,t) = G\delta(x - s(t))$$

which has the value of zero everywhere except at $x = s(t)$ (the location of the wetting front) and has an area of G $[\mathrm{W/m^2}]$.

To physically determine the magnitude of G, we consider the amount of heat liberated due to the heat of wetting in a differential slab of length ds in the x direction. This differential heat dQ [J] is given by $dQ = dmH$, where H is the heat of wetting and dm is the mass of the differential slab [kg], equivalent to ρdV (dV is the differential slab volume $[\mathrm{m^3}]$), leading to $dQ = \rho dVH$. The volume of the differential slab is $dV = Ads$ where A is the cross-sectional area of the slab, which gives $dQ = \rho AHds$. The heat per unit area is then given by $dQ/A = pHds$. The time rate of heat (i.e., power) produced per unit area is simply the time required for the wetting front to pass through this slab, dt; $G = (dQ/dt)/A = \rho Hds/dt$. This is in fact, the same expression for the heat produced at the interface in the Stefan problem. However, previously it was incorporated into the Stefan condition rather than as the magnitude of a Dirac delta heat source. This results in a heat source given by

$$g_{LH}(x,t) = \rho H\frac{ds}{dt}\delta(x - s(t))$$

The height of the wetting front is known to be proportional to the square root of time, so the position of the wetting front is $s(t) = u\sqrt{t}$ where $u \propto S$ is proportional to the sorptivity $[\mathrm{m}/\sqrt{\mathrm{s}}]$. This results in a heat source of

$$g_{LH}(x,t) = \rho H\frac{u}{2\sqrt{t}}\delta(x - u\sqrt{t})$$

The next two subsections illustrate two different solution methods for solving this system of governing equations with source term and boundary conditions. First, we solved the system using Laplace transforms.

4.3.1. Laplace Transform Solution Method

Taking the Laplace Transform of the governing equation and the boundary conditions results in the following subsidiary equations

$$\frac{d^2\overline{T}}{dx^2}+\frac{1}{k}\rho H\int_0^\infty e^{-pt}\frac{u}{2\sqrt{t}}\delta(x-u\sqrt{t})\,\mathrm{d}t=\frac{1}{\alpha_T}p\overline{T}+\frac{Ph}{kA}\overline{T}$$

$$-k\frac{\partial\overline{T}}{\partial x}(0,p)+h_1\overline{T}=0,$$

$$k\frac{\partial\overline{T}}{\partial x}(L,p)+h_2\overline{T}=0,$$

Where p is the Laplace transform parameter and an overbar indicates a Laplace-transformed variable. Using the substitution $\tau=-\,u\sqrt{t},\ d\tau=-\frac{u}{2\sqrt{t}}dt$ the Laplace transform of the Delta function can be found as

$$=-\int_0^{-\infty} e^{-p\left(\frac{\tau}{u}\right)^2}\delta(\tau+x)\,\mathrm{d}\tau$$

$$=\int_{-\infty}^{0} e^{-p\left(\frac{\tau}{u}\right)^2}\delta(\tau-(-x))\,\mathrm{d}\tau$$

using the property of the Dirac delta function shown in Equation (4a),

$$\int_{-\infty}^{0} e^{-p\left(\frac{\tau}{u}\right)^2}\delta(\tau-(-x))\,\mathrm{d}\tau=e^{-p\left(\frac{x}{u}\right)^2}.$$

Thus, the subsidiary equation becomes

$$\frac{d^2\overline{T}}{dx^2}+\frac{\rho H}{k}e^{-p\left(\frac{x}{u}\right)^2}=\left(\frac{p}{\alpha_T}+\frac{Ph}{kA}\right)\overline{T}$$

Using Mathematica (Wolfram, 2021) and the mpmath Python library (Johansson et al., 2017), the governing equation and associated boundary conditions were posed in Laplace space and numerically inverted back to the time domain. The behavior for select types of boundary conditions are shown in Figure 11.

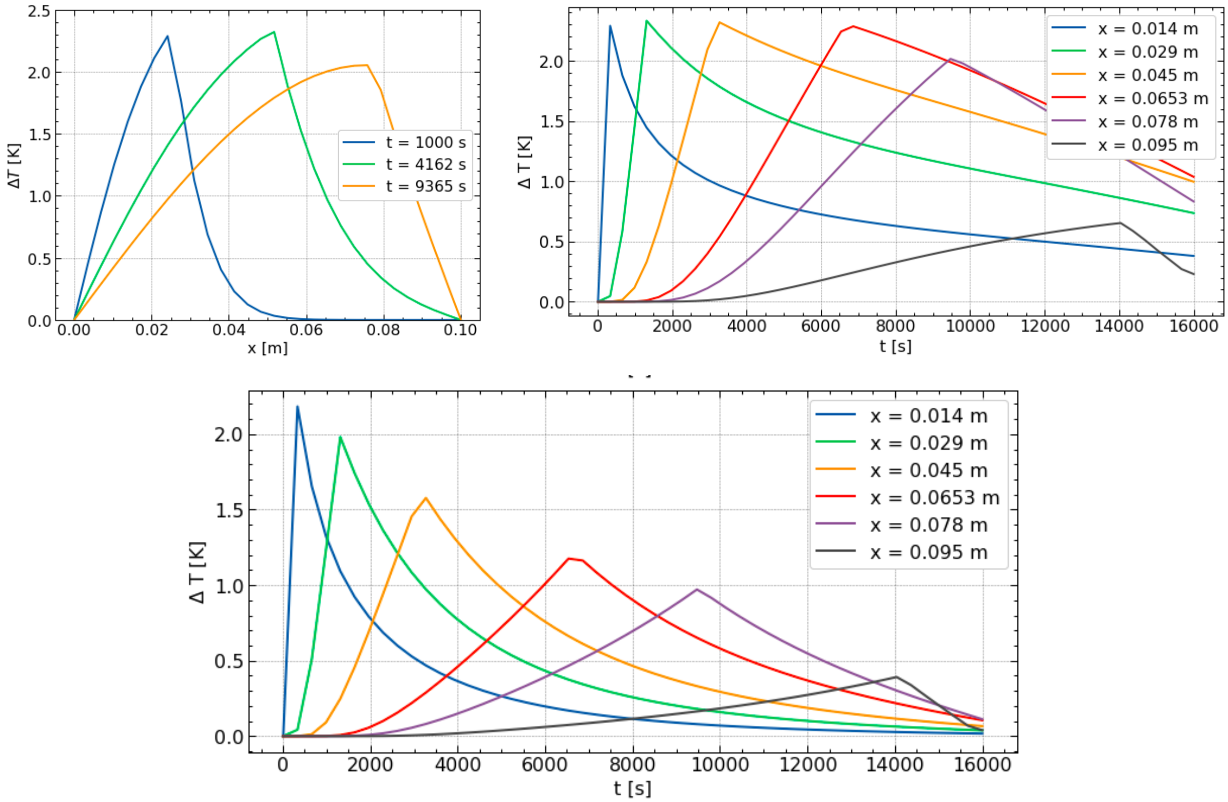

Figure 11. Temperature rise predicted by hybrid Stefan/point source approach; space profiles (top left); time profile without heat loss (top right); time profile with non-zero heat loss on sides of core (bottom)

In contrast to the Neumann solution of the original Stefan problem, the temperature at the interface (the temperature of the peak) is not constant, but decays over time. This can be partially attributed to the heat loss at the end boundary $(x = L)$, which the Neumann solution does not include. In the case with no heat loss to the cylindrical boundary, for values of $x \ll L$, this solution resembles the Neumann solution. However, as x approaches L, the temperature at the interface significantly decreases as more heat is lost at the boundary $x = L$. In the case with a moderate amount of heat loss to the circumferential boundary, the temperature at the interface decreases gradually as x increases and decreases abruptly as x approaches L. This trend in the temperature of the peaks can be somewhat observed in the zeolitic tuff data, although other effects such as evaporative cooling and variation in the surrounding temperature add uncertainty to the later time data.

This solution is not only a solution to the imbibition problem but can also be thought of as a solution to the finite domain Stefan problem with a known equation for the position of the interface. Whereas in the Neumann solution the temperature at the interface was known and the position of the wetting front was determined, using this formulation, the position of the wetting front is known and the temperature at the interface is determined.

The next sub-section presents an alternative method for solution to the hybrid Stefan/Dirac delta problem using a Green's function approach, rather than a Laplace transform that requires a numerical Laplace transform inversion.

4.3.2. Green's Function Solution Method

This same conceptual problem can be solved with the use of Green's functions, rather than Laplace transforms. The one-dimensional transient heat conduction equation on the region $0 \leq x \leq L$ with heat loss to the cylindrical boundary with Dirichlet boundary conditions is formulated as

$$\frac{\partial^2 T}{\partial x^2} + \frac{1}{k} g_{LH}(x,t) = \frac{1}{\alpha_T} \frac{\partial T}{\partial t} + \frac{Ph}{Ak} T$$

$$T(0,t) = f_1(t)$$

$$T(L,t) = f_2(t)$$

$$T(x,0) = F(x).$$

This problem has the solution, using the method of Green's functions (Özişik, 1993), of

$$\begin{aligned} &T(x,t) \\ &\quad = \int_{x'=0}^{L} G(x,t \,|\, x',\tau)|_{\tau=0} F(x') \, \mathrm{d}x' + \frac{\alpha}{k} \int_{\tau=0}^{t} \mathrm{d}\tau \int_{x'=0}^{L} G(x,t \,|\, x',\tau) g_{LH}(x',\tau) \, \mathrm{d}x' + \alpha \\ &\quad \int_{\tau=0}^{t} \left. \frac{\partial G(x,t \,|\, x',\tau)}{\partial x'} \right|_{x=0}^{\prime} f_1(\tau) \, \mathrm{d}\tau - \alpha \int_{\tau=0}^{t} \left. \frac{\partial G(x,t \,|\, x',\tau)}{\partial x'} \right|_{x'=L} f_2(\tau) \, \mathrm{d}\tau \end{aligned}$$

where the Green's Function for the above partial differential equation is

$$G(x,t \,|\, x',\tau) = \frac{2}{L} \sum_{m=1}^{\infty} e^{-\alpha_T \left(\beta_m^2 + \frac{Ph}{Ak}\right)(t-\tau)} \sin(\beta_m x) \sin{(\beta_m x')} \; ; \; \beta_m = \frac{m\pi}{L}.$$

For the case when the boundary behaviors are constant with time and zero ($f_1(t) = 0$, $f_2(t) = 0$, and $F(x) = 0$), the solution simplifies to

$$T(x,t) = \frac{2\alpha}{kL} \sum_{m=1}^{\infty} e^{-\alpha_T \left(\beta_m^2 + \frac{Ph}{Ak}\right)t} \sin(\beta_m x) \int_{\tau=0}^{t} e^{\alpha_T \left(\beta_m^2 + \frac{Ph}{Ak}\right)\tau} \int_{x'=0}^{L} \sin{(\beta_m x')} \, g_{LH}(x',\tau) \, \mathrm{d}x' \, \mathrm{d}\tau \,.$$

Given the heat source term of $g_{LH}(x,t) = \rho H \frac{u}{2\sqrt{t}} \delta(x - u\sqrt{t})$, the integral with respect to x' becomes

$$\begin{aligned} &\int_{x'=0}^{L} \sin{(\beta_m x')} \, \rho H \frac{u}{2\sqrt{\tau}} \delta(x' - u\sqrt{\tau}) \, \mathrm{d}x' \\ &= \rho H \frac{u}{2\sqrt{\tau}} \int_{x'=0}^{L} \sin{(\beta_m x')} \, \delta(x' - u\sqrt{\tau}) \, \mathrm{d}x' \\ &= \rho H \frac{u}{2\sqrt{\tau}} \sin{(\beta_m u\sqrt{\tau})} \end{aligned}$$

This results in an updated solution of

$$T(x,t) = \frac{u\alpha\rho H}{Lk}\sum_{m=1}^{\infty} e^{-\alpha_T\left(\beta_m^2+\frac{Ph}{Ak}\right)t}\sin(\beta_m x)\int_{\tau=0}^{t} e^{\alpha_T\left(\beta_m^2+\frac{Ph}{Ak}\right)\tau}\frac{\sin\,(\beta_m u\sqrt{\tau})}{\sqrt{\tau}}\,\mathrm{d}\tau\,.$$

The integral can be evaluated as

$$\int_{\tau=0}^{t} e^{\alpha_T\left(\beta_m^2+\frac{Ph}{Ak}\right)\tau}\frac{\sin\,(\beta_m u\sqrt{\tau})}{\sqrt{\tau}}\,\mathrm{d}\tau$$
$$= e^{\left(\frac{\beta_m u}{2\varepsilon_m}\right)^2}\frac{\sqrt{\pi}}{\varepsilon_m}\left\{\Re\left[\operatorname{erf}\left(\frac{\beta_m u}{2\varepsilon_m}+i\varepsilon_m\sqrt{t}\right)\right]-\operatorname{erf}\left(\frac{\beta_m u}{2\varepsilon_m}\right)\right\}$$

where i is the imaginary unit, $\Re$ indicates the real component of the complex term, and $\varepsilon_m = \sqrt{\alpha_T\left(\beta_m^2+\frac{Ph}{Ak}\right)}$. This results in the final closed-form solution:

$$T(x,t) = \frac{u\alpha_T\rho H\sqrt{\pi}}{Lk}\sum_{m=1}^{\infty} e^{-\varepsilon_m^2 t}\sin(\beta_m x)\,e^{\left(\frac{\beta_m u}{2\varepsilon_m}\right)^2}\frac{1}{\varepsilon_m}\left\{\Re\left[\operatorname{erf}\left(\frac{\beta_m u}{2\varepsilon_m}+i\varepsilon_m\sqrt{t}\right)\right]-\operatorname{erf}\left(\frac{\beta_m u}{2\varepsilon_m}\right)\right\}.$$

To evaluate this solution, the infinite sum is truncated at N, where N is large enough for the sum to converge ($N = 50$ was found to be sufficient in most cases). In mpmath, Richardson extrapolation is used to accelerate the sum and approximate the infinite sum in fewer terms.

An analytical solution for the above problem with third type (Robin) boundary conditions is also obtainable using a Green's Function. However, the eigenvalues β_m must be determined as the root of a transcendental equation, which is more difficult to compute when ~50 eigenvalues must be calculated. Regardless, homogenous Dirichlet boundary conditions are currently an adequate approximation for the experimental conditions presented earlier.

This Green's function solution is equivalent to the solution found via the numerical inverse transform but is faster to evaluate numerically, has no issues with evaluating at $t = 0$ (unlike the Laplace transform approach, where $t \to 0$ corresponds to $p \to \infty$), and produces the same curves shown in Figure 11.

4.3.3. Nondimensionalization

The problem can be formulated in terms of the dimensionless variables

$$\chi = \frac{x}{L};\quad \tau = \frac{\alpha_T t}{L^2};\quad \theta = \frac{kT}{\rho\alpha_T H} = \frac{c_p T}{H}\,.$$

The transformations for x and t are standard dimensionless transformations for heat conduction problems, while the transformation of T uses a reference temperature of H/c_p. This can be thought of as the rise of temperature of an infinitesimal slice of the rock due to the heat of wetting H in the region, which is useful when the initial conditions and both boundary conditions are zero. These transformations reduce the governing partial differential equation to

$$\frac{\partial^2\theta}{\partial\chi^2}+\frac{v}{2\sqrt{\tau}}\delta(\chi - v\sqrt{\tau}) = \frac{\partial\theta}{\partial\tau}+C\theta;\qquad 0<\chi<1,\ 0<\tau<\frac{1}{v^2}$$

with the use of the property of the Dirac delta function given by Equation 4b, and where $v = \frac{u}{\sqrt{\alpha}}$ and $C = \frac{PhL^2}{Ak}$ are dimensionless parameters. In terms of the dimensionless parameters, the solution is

$$\theta(\chi,\tau) = v\sqrt{\pi}\sum_{m=1}^{\infty}\frac{1}{\varepsilon_m}e^{\left(\frac{\beta_m v}{2\varepsilon_m}\right)^2}e^{-\varepsilon_m^2\tau}\sin(\beta_m\chi)\left\{\Re\left[\mathrm{erf}\left(\frac{\beta_m v}{2\varepsilon_m}+i\varepsilon_m\sqrt{\tau}\right)\right]-\mathrm{erf}\left(\frac{\beta_m v}{2\varepsilon_m}\right)\right\}$$

where $\beta_m = m\pi$ and $\varepsilon_m = \sqrt{\beta_m^2 + C}$.

The parameter v is the ratio of the wetting front speed scaled to a square-root time axis (i.e., with the units of sorptivity) and the square root of the thermal diffusivity. In soil science, the typical interpretation of imbibition tests is $I = S\sqrt{t}$, where I is the infiltration $[\mathrm{m/s}]$ (volume of water imbibed, divided by the cross-sectional area of the sample) and sorptivity (S) the slope with units $\mathrm{m}/\sqrt{\mathrm{s}}$. This dimensionless quantity v is therefore a type of hydrological-thermal Péclet number (i.e., advection/diffusion), which illustrates the balance of water advection and thermal diffusion. The analytical solution only takes diffusion into account, so it would be inappropriate for large v, where the convection of heat would be significant compared to the diffusion of heat.

The parameter C quantifies balance between heat loss to the sides of the sample (Ph) and heat conduction down the length of the sample (Ak). The term is proportional to the Biot number. If heat loss to the surroundings is larger than conduction in the rock, the dimensionless source term coefficient becomes large. A small value of C would be characteristic of a well-insulated one-dimensional core.

5. CONCLUSIONS AND NEXT STEPS

This report gives a status update on further advances in a new laboratory testing approach that uses temperatures to track the wetting front during imbibition. We present both an analytical solution to be used for matching to the observed thermal pulse, and an alternative conceptualization (multi-modal capillary pressure curve) to recreate both the observed early- and late-time slopes in the mass imbibed curves during imbibition tests.

The alternative conceptual models for double-porosity fluid flow can both re-create the observed behavior in core-scale lab tests. The multicontinuum approach (Kuhlman et al., 2022b) is more general, but the multi-modal flow approach (given here) is more efficient at the core scale investigated here. Their efficiency and ability to properly capture the relevant physics of fluid flow at the field scale must still be investigated.

An analytical solution was developed for the heat transfer problem introduced in first FY22 progress report. This analytical solution is the first analytical solution we know of to explain this phenomenon observed in our laboratory and reported previously in the literature in paper and other porous media.

A drainage testing capability has been procured for performing tests using a small laboratory centrifuge. This capability will be used in the next fiscal year to investigate the two-phase flow properties of rocks that have permeabilities too low to test with imbibition methods; also, the drainage capability may better examine larger pores than the imbibition methods that are most sensitive to smaller pores.

REFERENCES

Aslannejad, H., A. Terzis, S.M. Hassanizadeh & B. Weigand, 2017. Occurrence of temperature spikes at a wetting front during spontaneous imbibition, *Scientific Reports, 7*:7268.

Edlefsen, N.E. & A.B.C. Anderson, 1943. Thermodynamics of soil moisture, *Hilgardia, 15*(2):31-298.

Heath, J.E., K.L. Kuhlman, S.T. Broome, J.E. Wilson & B. Malama, 2021. Heterogeneous multiphase flow properties of volcanic rocks and implications for noble gas transport from underground nuclear explosions, *Vadose Zone Journal, 20*(3):e20123.

Johansson, F., V. Steinberg, S.B. Kirpichev, K.L. Kuhlman, A. Meurer, O. Čertík, C. Van Horsen, P. Masson, J. Arias de Reyna, T. Hartmann, M. Kagalenko, P. Peterson, Z. Jędrzejewski-Szmek, S. Krastanov, J. Warner, W. Weckesser, T. Buchert, N. Schlömer, J. Creus-Costa, G.-L. Ingold, C. Behan & A. Brys, 2017. *mpmath: a Python library for arbitrary-precision floating-point arithmetic*. https://mpmath.org/

Kuhlman, K.L., J.E. Heath & S.T. Broome, 2020. *FY20 Two-Phase Flow for Containment Science in LYNM*, (52 p.) SAND2020-10521, Albuquerque, NM: Sandia National Laboratories.

Kuhlman, K.L. & J.E. Heath, 2021. *Multicontinuum Flow Models for Assessing Two-Phase Flow in Containments Science*, (67 p.) SAND2021-7191, Albuquerque, NM: Sandia National Laboratories.

Kuhlman, K.L., M.M. Mills, J.E. Heath, M.J Paul, J.E. Wilson & J.E. Bower, 2021. *Spontaneous Imbibition Tests and Parameter Estimation in Volcanic Tuff*, (63 p.) SAND2021-9640, Albuquerque, NM: Sandia National Laboratories.

Kuhlman, K.L., M.M. Mills, J.E. Heath, M.J. Paul, J.E. Wilson & J.E. Bower, 2022a. Parameter estimation from spontaneous imbibition into volcanic tuff, *Vadose Zone Journal, 21*(2):e20188.

Kuhlman, K.L., M.M. Mills, J.E. Heath & M.J. Paul, 2022b. *FY22 Progress on Multicontinuum Methods in Containment*, (30 p.) SAND2022-10011, Albuquerque, NM: Sandia National Laboratories.

Murali, V., J.C.H. Zeegers & A.A. Darhuber, 2020. Infrared thermography of sorptive heating of thin porous media – Experiments and continuum simulations, *International Journal of Heat and Mass Transfer, 147*(118875):1-10.

NIST, 2022. *Digital Library of Mathematical Functions*. http://dlmf.nist.gov/, Release 1.1.6 of 2022-06-30. F.W.J. Olver, A.B. Olde Daalhuis, D.W. Lozier, B.I. Schneider, R.F. Boisvert, C.W. Clark, B.R. Miller, B.V. Saunders, H.S. Cohl & M. A. McClain, eds.

Özişik, N.M., 1993. *Heat Conduction*, second edition. John Wiley.

Parker, J. C., Lenhard, R. J., & Kuppusamy, T. (1987). A parametric model for constitutive properties governing multiphase flow in porous media. *Water Resources Research, 23*(4), 618–624.

Peters, R.R. & E.A. Klavetter, 1988. A continuum model for water movement in an unsaturated fractured rock mass, *Water Resources Research, 24*(3):416-430.

Peters, R.R., E.A. Klavetter, J.T. George & J.H. Gauthier, 1987. "Measuring and modeling water imbibition into tuff" in D.D. Evans & T.J. Nicholson [Eds.] *Flow and Transport Through Unsaturated Fractured Rock*, pp. 99-106. AGU Monograph 42.

Philip, J.R., 1957. The theory of infiltration: 4 Sorptivity and algebraic infiltration equations, *Soil Science, 84*(3):257-264.

Richards, L.A., 1931. Capillary conduction of liquids through porous mediums, *Physics, 1*(5):318-333.

Somerton, W.H., J.A. Keese & S.L. Chu, 1974. Thermal behavior of unconsolidated oil sands, *Society of Petroleum Engineers Journal, 14*(5):513-521.

Tokunaga, T.K., 2020. Simplified Green-Ampt model, imbibition-based estimates of permeability, and implications for leak-off in hydraulic fracturing, *Water Resources Research, 56*:e2019WR026919.

Tokunaga, T.K. & J. Wan, 1997. Water film flow along fracture surfaces of porous rock, *Water Resources Research, 33*(6):1287-1295.

van Genuchten, M.Th., 1980. A closed-form equation for predicting the hydraulic conductivity of unsaturated soils, *Soil Science Society of America Journal, 44*(5):892-899.

Wolfram Research, Inc., 2021. *Mathematica Version 12.3*, Champaign, IL.

DISTRIBUTION

Email—Internal

Name	Org.	Sandia Email Address
Scott Broome	8914	stbroom@sandia.gov
Chris Camphouse	8842	rccamph@sandia.gov
Austin Holland	8914	aaholla@sandia.gov
Technical Library	1911	sanddocs@sandia.gov

This page left blank